JAMES | Journal of Advances in Modeling Earth Systems®

RESEARCH ARTICLE
10.1029/2022MS003226

Key Points:

- Even with feedbacks constrained, ice mass varies 5-fold with structural differences in cirrus microphysics
- These differences develop rapidly within trajectory lifetime due to differences in representations of ice nucleation
- Three cirrus lifecycles with distinct radiative signatures are proposed

Correspondence to:
S. Sullivan,
sylvia@arizona.edu

Citation:
Sullivan, S., Voigt, A., Miltenberger, A., Rolf, C., & Krämer, M. (2022). A Lagrangian perspective of microphysical impact on ice cloud evolution and radiative heating. *Journal of Advances in Modeling Earth Systems*, *14*, e2022MS003226. https://doi.org/10.1029/2022MS003226

Received 1 JUN 2022
Accepted 20 OCT 2022

Author Contributions:
Conceptualization: A. Voigt
Funding acquisition: A. Voigt
Methodology: A. Voigt, A. Miltenberger, C. Rolf, M. Krämer
Project Administration: A. Voigt
Software: A. Miltenberger, C. Rolf
Writing – review & editing: A. Voigt, A. Miltenberger, C. Rolf, M. Krämer

A Lagrangian Perspective of Microphysical Impact on Ice Cloud Evolution and Radiative Heating

S. Sullivan[1,2], A. Voigt[3], A. Miltenberger[4], C. Rolf[5], and M. Krämer[4,5]

[1]Department of Chemical and Environmental Engineering, University of Arizona, Tucson, Arizona, US, [2]Institute for Meteorology and Climate Research, Karlsruhe Institute of Technology, Karlsruhe, Germany, [3]Department of Meteorology and Geophysics, University of Vienna, Vienna, Austria, [4]Johannes Gutenberg University of Mainz, Mainz, Germany, [5]Forschungzentrum Jülich, Jülich, Germany

Abstract We generate trajectories in storm-resolving simulations in order to quantify the effect of ice microphysics on tropical upper-tropospheric cloud-radiative heating. The pressure and flow field tracked along the trajectories are used to run different ice microphysical schemes, both one- and two-moment formulations within the Icosahedral Non-hydrostatic Model model and a separate offline box microphysics model (CLaMS-Ice). This computational approach allows us to isolate purely microphysical differences in a variant of "microphysical piggybacking;" feedbacks of microphysics onto pressure and the flow field, for example, via latent heating, are suppressed. Despite these constraints, we find about a 5-fold difference in median cloud ice mass mixing ratios (q_i) and ice crystal number (N_i) between the microphysical schemes and very distinct q_i distributions versus temperature and relative humidity with respect to ice along the trajectories. After investigating microphysical formulations for nucleation, depositional growth, and sedimentation, we propose three cirrus lifecycles: a *weak source-strong sink* lifecycle whose longwave and shortwave heating are smallest due to short lifetime and low optical depth, a *strong source-weak sink* lifecycle whose longwave and shortwave heating are largest due to long lifetime and high optical depth, and a *strong source-strong sink* lifecycle with intermediate radiative properties.

Plain Language Summary The number and mass of ice crystals in upper-level clouds affect how much infrared radiation these clouds absorb and how much sunlight they reflect. Changing the description of how these crystals form and grow in models directly alters the crystal number and mass. But it can also indirectly alter the number and mass by changing temperature or available moisture via, for example, latent heating. We control for these indirect changes by using the same set of variables to run different models of ice crystal formation and growth. Even with the indirect changes suppressed, we produce a large variation in the number and mass of ice crystals with different models. We dig into why this is by looking at parameters describing crystal formation, growth, and sedimentation. The strength of these three processes generates distinct ice cloud lifecycles for which infrared radiation and sunlight are also absorbed and reflected with differing strength.

1. Introduction

With atmospheric models transitioning toward high-resolution, storm-resolving setups, their output fidelity will increasingly depend on our representation of processes at the smallest scales. Deep convection no longer needs to be parameterized within these storm-resolving models, as the horizontal resolution is sufficient to explicitly represent it (e.g., Satoh et al., 2019; Stevens et al., 2020; Wedi et al., 2020). However, parameterizations of cloud microphysics—processes like ice crystal nucleation, aggregation, and sedimentation—remain. Ice-phase microphysics represents a unique challenge, as crystals involve complex geometries and optical properties, as well as formation on a very specific subset of atmospheric aerosol (e.g., Järvinen et al., 2018; Kanji et al., 2017; Lawson et al., 2019).

Ice crystals absorb outgoing infrared radiation and reflect incoming solar radiation, generating an "in-cloud heating, cloud-top cooling dipole." Our recent work shows how influential small-scale ice microphysical properties are on this heating-cooling dipole over the Asian monsoon region at storm-resolving resolutions (Sullivan & Voigt, 2021): Factors like the ice crystal size and aerosol dependence of ice formation can change the magnitude of cloud-radiative heating ($\mathcal{H}$) 4-fold. Such differences in $\mathcal{H}$ affect the large-scale circulation, for example, via the

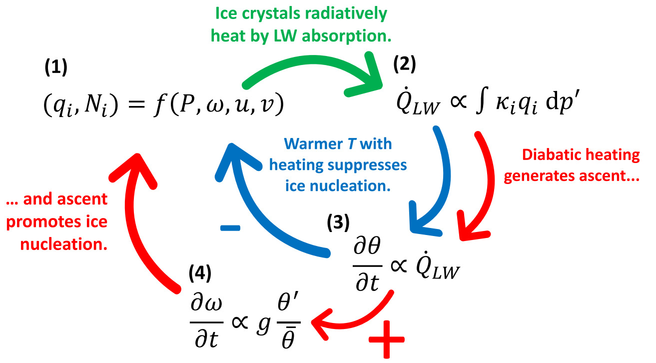

Figure 1. The focus here is on Equation 1, investigated in a series of microphysical analyses, and the green arrow, evaluated in radiative scalings for characteristic ice clouds. Cloud ice mass mixing ratio (q_i) and crystal number (N_i) are predicted in the microphysics scheme as a function of temperature and pressure among other variables (T and P, **1**). The vertical integral of this cloud ice mass and the absorption cross-section of ice (κ_i) determines longwave radiative heating ($\dot{Q}_{\mathrm{LW}}$, **2**). This heating affects potential temperature (θ) and hence pressure velocity (ω, **3** and **4**). Warmer temperatures suppress ice nucleation (blue) but also promote buoyant ascent which dynamically enhances ice nucleation (red). Our approach turns off the red pathway.

latitudinal extent of the Hadley circulation or the longitudinal position of the Walker cells (e.g., Schumacher et al., 2004; Voigt et al., 2019).

We build upon the results of Sullivan and Voigt (2021) here, further investigating the ice microphysical control on tropical $\mathcal{H}$ with airmass trajectories. Trajectories provide a means of isolating the direct microphysical effect from the indirect microphysical-dynamic feedbacks. *Direct microphysical effect* refers to how much liquid or ice condensate a given microphysics scheme produces for a given pressure and flow field ((1) in Figure 1). *Indirect microphysical-dynamic feedback* means how microphysics changes the flow field through diabatic heating, generating additional ascent (red arrows in Figure 1). Examples of such feedbacks are more common for the latent than radiative heating component of diabatic heating. Two convective invigoration hypotheses propose that lofting of condensate above the freezing level and reduction of supersaturation by cloud droplets intensify updrafts via additional latent heating (Fan et al., 2007; Rosenfeld et al., 2008).

Several studies have already isolated these direct versus indirect microphysical impacts with a methodology referred to as piggybacking (e.g., Grabowski, 2014, 2019). *Piggybacking* employs two sets of thermodynamic variables, one allowing the microphysics to feed back on the flow field through buoyancy and the other only responding passively to this flow field, that is, piggybacking upon it. Grabowski (2015) and Grabowski and Morrison (2016) used this methodology within deep convection to explore the validity of the convective invigoration hypothesis, and Grabowski and Jarecka (2015) and Grabowski and Morrison (2017) used it to explore the effect of saturation adjustment versus saturation tracking in shallow and deep convection. Here, we have tracked thermodynamic state and flow field along our trajectories and compare output of online microphysics to that of a second offline microphysics model. Our technique is similar to that of Grabwoski but more restrictive. The only element changing between runs is the microphysics scheme, whereas in traditional piggybacking, the entire model infrastructure, including radiation and advection schemes, is run with a separate set of thermodynamics but the same dynamics.

Trajectories allow quantification of how much cloud ice mass and number can change in the absence of microphysical-dynamic feedbacks and to estimate the resultant change in tropical $\mathcal{H}$. Aside from their utility as a variant of microphysical piggybacking, trajectories are a natural tool to study spatiotemporally persistent ice clouds. They have been previously used to assess the impact of aerosol and cooling rate on thin cirrus optical depth or more recently to understand anvil cirrus lifecycle (e.g., Brabec et al., 2012; Gasparini et al., 2021; Haag & Kärcher, 2004; Kienast-Sjögren et al., 2015). Most recently, trajectory analysis has been used in combination with data of the Stratospheric and upper tropospheric processes for better climate predictions campaign (StratoClim) to highlight the importance of overshooting convection in setting stratospheric water vapor concentrations over the Asian monsoon area (Khaykin et al., 2021).

The focus here is on the same Asian monsoon domain and StratoClim time period. Two sets of trajectories are generated in a storm-resolving model, and their thermodynamic variables and flow fields are used to produce six sets of ice cloud microphysical characteristics. Variability in these simulated ice clouds is first quantified, both statistically and as a function of trajectory lifetime. We then evaluate their thermodynamic dependence and examine differences in process formulations for phases of ice cloud evolution. Based on these analyses, we propose three lifecycle types and perform scaling for the associated range in cloud-radiative heating with feedbacks constrained.

2. Methods

2.1. Storm-Resolving Simulations

The Icosahedral Non-hydrostatic Model (ICON) version 2.3.0 of the German Weather Service is run between 5 August 2017 12:00 UTC and 9 August 2017 00:00 UTC in a limited-area domain over the Asian monsoon region from 55°E to 115°E and 5°S to 40°N (Figure 2a). We use a 24-s time step and a 2.5-km equivalent resolution

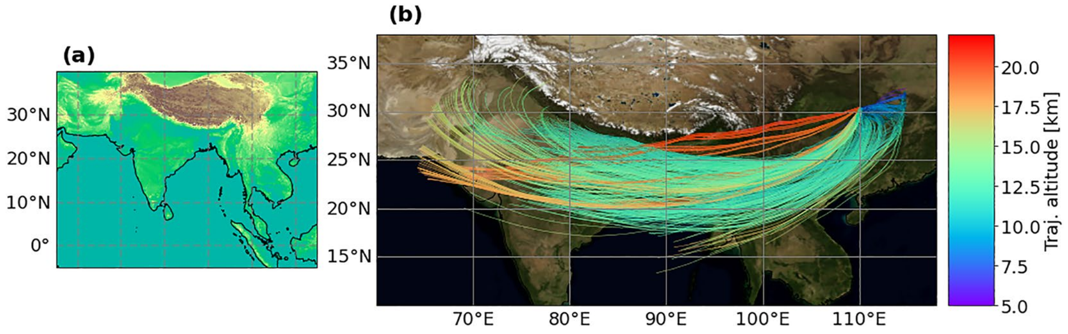

Figure 2. Trajectories initialize in the Sichuan basin and move westward over the Bay of Bengal and India. Simulation domain over the Asian monsoon region (panel a). Fifty one-hour-long trajectories from a single initialization time and single output file colored by associated altitude (panel b).

(R2B10 icosahedral grid) for which deep convection should be explicitly represented. Shallow convection is still parameterized as in Nordeng (1994). The Integrated Forecast System provides initial and lateral boundary conditions, the latter every 3 hr with analysis values at 00:00 and 12:00 UTC and forecast values in between. The German Weather Service provides surface and aerosol data. The default 75 vertical levels up to 30 km are used with a grid spacing of 500 m in the upper troposphere, as our previous work indicates limited impact of increasing this vertical resolution, even in the upper troposphere (Sullivan & Voigt, 2021). Trajectories are computed within this base ICON setup.

2.1.1. Online Trajectories

A module has recently been implemented into the ICON model to evaluate trajectories using the resolved-scale wind fields at each model time step (Miltenberger et al., 2020). The trajectory equation is solved using an implicit Euler scheme, and interpolation of wind and trace variables to the trajectory position is done on the native unstructured ICON grid. Within our simulations, trajectories are initiated at 09:00 UTC on 6 August 2017 at all half levels between 8 and 22 km in a patch from 30°N to 32°N and from 108.5°E to 110.5°E for a total of about 20,000 trajectories in each set (Figure 2b, where a subset of 700 trajectories is shown). This initial geographic patch is chosen on the basis of Lee et al. (2019) who tracked formation of moist and ice layers near the tropopause back to overshooting convection in the Sichuan Basin. The trajectories evolve over 51 hr, primarily toward the western half of the simulation domain. Importantly, our trajectories have the same 24-s time step as ICON. Earlier studies indicate the need for this high temporal resolution in representing wind and temperature fluctuations in the upper troposphere (e.g., Kienast-Sjögren et al., 2015; Miltenberger et al., 2013).

Along these trajectories, the following thermodynamic and microphysical variables are tracked: density, temperature, pressure, specific humidity, cloud ice mass and number mixing ratios, cloud liquid mass and number mixing ratios, graupel mass and number mixing ratios, and ice sedimentation mass and number mixing ratios both into and out of the parcel. We run two ICON simulations with these online trajectories, one with the operational one-moment microphysics scheme of Doms et al. (2005) denoted "1M" throughout and one with the two-moment scheme of Seifert and Beheng (2006) denoted "2M" throughout (Table 1).

2.2. CLaMS-Ice Box Model

The Chemical Lagrangian Model of the Stratosphere is a 3D trajectory module (McKenna et al., 2002) that can be coupled with the two-moment ice microphysics of Spichtinger and Gierens (2009). The combined model is called CLaMS-Ice and acts as our offline box model for comparison to ICON microphysics. CLaMS-Ice represents homogeneous and heterogeneous ice nucleation, depositional growth and sublimation, aggregation, and sedimentation, in greater detail than the one-moment microphysics of ICON.

Importantly, CLaMS-Ice describes only ice-phase processes and operates only for temperatures colder than 235 K. If we compare trajectories with the same inputs then, that is, either the "1M" or "2M" sets, we see the effect of ice-only microphysics, as the mixed-phase microphysics for $T > 235$ K is the same. Heterogeneously formed ice crystals are only included in CLaMS-Ice if there is no preexisting cloud ice when the simulation starts at 235 K;

Table 1
The Trajectory Naming Scheme Uses One Prefix to Designate Either **C***LaMS-Ice or* **I***CON and Three Suffixes to Designate Settings*

Designation	Simulation setting
C_	Offline CLaMS-Ice microphysics as in Spichtinger and Gierens (2009)
I_	Online ICON microphysics as in Doms et al. (2005) or Seifert and Beheng (2006)
_M	1 = ICON one-moment microphysics as in Doms et al. (2005)
	2 = ICON two-moment microphysics as in Seifert and Beheng (2006)
_T	0 = temperature fluctuation/gravity wave parameterization off
	1 = temperature fluctuation parameterization on as in Podglajen et al. (2016)
_S	0 = pseudo-mixing to conserve total water as in Equation 3 off
	1 = pseudo-mixing to conserve total water on as in Equation 3

Note. The temperature fluctuation parameterization and pseudo-mixing tendency are always turned off in the ICON trajectories, that is, they are always “0T0S.”

INP are assumed to be very efficient, so that the presence of a preexisting ice cloud indicates that all INP have been activated. Along the one-moment trajectories, CLaMS-Ice receives q_i but not N_i from ICON at 235 K. N_i is prescribed using the IWC-D_e parameterization of Boudala et al. (2002), based upon in situ measurements from four flights of ice water content and crystal cross-sectional area from the Nevzorov and 2DC probes respectively.

CLaMS-Ice assumes columnar ice crystals and does not differentiate between ice and snow. The ice crystal and aerosol size distributions are assumed to be lognormal with their first two moments tracked. Additionally, the cloud ice is broken down into three “freezing classes”—heterogeneously nucleated, homogeneously nucleated, and preexisting cloud ice—whose first two moments are also tracked. At each time step, the prognostic equations are solved for the distribution moments, potential temperature, and specific humidity. Default parameters for CLaMS-Ice simulations are derived from optimizing the agreement between model output and freezing experiments of the AIDA cloud chamber (Baumgartner et al., 2022). Additional details of the CLaMS-Ice microphysics are discussed below in Section 4.1.

2.2.1. Offline Trajectories

CLaMS-Ice is initialized from the corresponding ICON simulation temperature, pressure, and specific humidity. Because CLaMS-Ice runs only for temperatures colder than 235 K, the ice formed at mixed-phase temperatures in ICON is classified as preexisting ice in its own freezing class. After the initial time step, the pressure along the ICON trajectory constrains the CLaMS-Ice simulation, and the CLaMS-Ice temperature can respond to adiabatic compression and expansion (coming externally from the trajectory pressure) and to its latent heating calculation when ice forms (coming from an internal latent heating calculation).

In two sets of CLaMS-Ice trajectories, we activate a ***temperature fluctuation parameterization*** on the basis of superpressure balloon measurements in the PreConcordiasi campaign (Podglajen et al., 2016). These sets are denoted “1T” whereas sets without temperature fluctuations are denoted “0T” (Table 1). The temperature fluctuation parameterization is an Autoregressive Integrated Moving Average model in which displacements ζ from one time step to the next are calculated as

$$\zeta'_{i+1} = \zeta'_i + W \cdot dt \tag{1}$$

With W representing a white noise process associated with vertical velocity fluctuations, whose variance (0.16 m s^{-1}) is derived from measurements. Very low frequency fluctuations (<2 days^{-1}) are removed with a high-pass filter. These displacement fluctuations are converted to temperature fluctuations along a dry adiabat in a hydrostatic atmosphere as follows:

$$T'_{i+1} = -\frac{g}{c_p}\zeta'_{i+1} \tag{2}$$

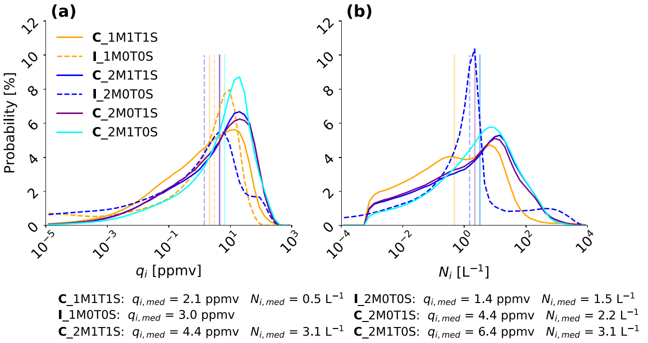

Figure 3. Ice crystal number distributions vary between Icosahedral Non-hydrostatic Model (ICON) and CLaMS-Ice trajectories more than ice mass mixing ratio distributions. Probability distributions of ice mass mixing ratio (panel a) and ice crystal number (panel b) for all time points of non-negligible ice cloud formation at cirrus temperatures ($q_i > 10^{-8}$ g kg^{-1}) along the trajectories. Table 1 explains the naming scheme; N_i is not recorded along the ICON one-moment trajectories. Distributions from trajectories driven by the one-moment microphysics in ICON are shown in orange, and those driven by the two-moment microphysics in shades of blue and purple. ICON distributions are in dashed lines, and CLaMS-Ice in solid. Median q_i and N_i values for each set are marked in the background and given below.

where g is gravitational acceleration and c_p is the isobaric heat capacity of air. Note that while temperature fluctuations also affect the vertical velocity under adiabatic expansion, this coupling cannot be accounted for along the trajectories as it would change the parcel position.

A final consideration is that total water in these offline CLaMS-Ice trajectories may differ from that in the online ICON ones because of processes other than ice microphysics, namely turbulent mixing of water vapor into or out of the trajectory parcel. We implement a ***pseudo-mixing term*** along the CLaMS-Ice trajectories to conserve total water relative to ICON:

$$q_{v,mix} = \left[q_v + q_c + q_s + q_i + q_g\right]_{i+1} - \left[q_v + q_c + q_s + q_i + q_g\right]_i - \left[q_{i,sedo} - q_{i,sedi}\right] \quad (3)$$

where q_v is specific humidity; q_c, q_s, q_i, and q_g are cloud liquid, snow, ice, and graupel mass mixing ratios; and $q_{i,sedo}$ and $q_{i,sedi}$ are the ice mass mixing ratios sedimenting out of and into the parcel as computed in the ICON simulations. The hail mass mixing ratios at the trajectory altitudes are negligible. The first term represents total water at time step $i + 1$, the second term represents total water at time step i, and the final term is net sedimentation of ice from the parcel. We neglect both sedimentation of q_c, as CLaMS-Ice runs at temperatures colder than 235 K, and of q_g and q_s, as they are an order-of-magnitude or more smaller than that of q_i. Trajectories that employ this pseudo-mixing term are denoted "1S" below.

3. Results

3.1. Distributions of Cloud Ice Properties

We begin with statistical comparisons of cloud ice mass mixing ratio (q_i) and ice crystal number concentration (N_i) along both the CLaMS-Ice and ICON trajectories for cirrus temperatures ($T < 237$ K, Figure 3). Using only the first 10% of each trajectory changes the distributions much more than using only 10% of the total number of trajectories. We take this to mean that a subset of anomalous trajectories is not distorting our distributions. Because these distributions tend to be skewed, we use the median as our metric of central tendency.

Median q_i varies by a factor of 4.5 between different sets of trajectories. Our limited-area simulations found an equivalent variation in mean q_i (Sullivan & Voigt, 2021). The trajectories indicate then that structural differences in ice microphysics are sufficient to generate such a spread in q_i. The two-moment trajectories differ more from one another than the one-moment ones, perhaps as the addition of uncertain parameters in more sophisticated schemes expands the space of possible cloud states (e.g., Morrison et al., 2020; Proske et al., 2021). Median N_i varies by a factor of six between sets of trajectories, and the N_i distributions exhibit quite different forms. The CLaMS-Ice trajectories all have a mean around 100 L^{-1} with significant spread (**C**_2M*). The ICON two-moment trajectories on the other hand exhibit a very strong, narrow mode at 10 L^{-1} (**I**_2M0T0S).

The temperature fluctuation parameterization does not significantly impact the q_i distribution from CLaMS-Ice (**C**_2M1T1S vs. **C**_2M0T1S). We are sampling primarily convective outflow rather than the in situ cirrus that are more sensitive to gravity waves. Inclusion of the pseudo-mixing term to conserve total water also reduces the tail of lower q_i values (**C**_2M1T1S vs. **C**_2M1T0S). This shift toward larger q_i values suggests that turbulent mixing of dry, ambient air suppresses nucleation of new small crystals or accelerates sublimation of thin cirrus. Because the temperature fluctuations and pseudo-mixing tendency do not drastically alter the q_i and N_i distributions, we focus on the one-versus two-moment and CLaMS-Ice versus ICON trajectories hereafter; this means using only the 1T1S trajectories from ClaMS-Ice (i.e., **C**_1M1T1S, **I**_1M0T0S, **C**_2M1T1S, and **I**_2M0T0S).

An advantage of analyzing microphysical sensitivity with offline CLaMS-Ice trajectories is that the model tracks its ice formation processes. In ICON, tracking process tendencies is more laborious and computationally expensive. From CLaMS-Ice process distributions, the large differences in q_i and N_i in Figure 3 come from preexisting ice, or ice formation in the mixed-phase regime (Figure 4). The two-moment trajectories contain an order of magnitude more preexisting ice mass and ice crystal number than the one-moment trajectories. Ice formation in

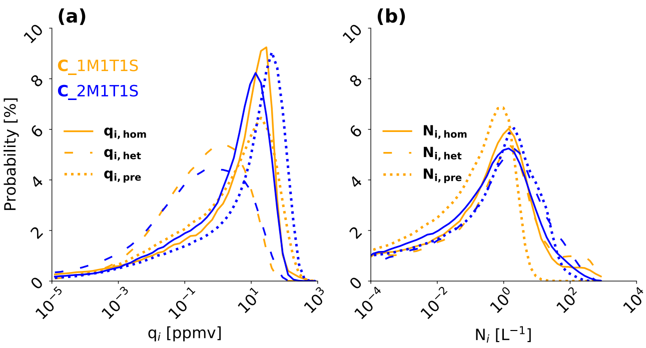

Figure 4. The preexisting cloud ice mass and ice crystal number differ most between the CLaMS-Ice one- and two-moment trajectories. Probability distributions of ice mass mixing ratio (panel a) and ice crystal number (panel b) generated by homogeneous nucleation (**hom**, solid line) or heterogeneous nucleation (**het**, dashed line) or preexisting in the parcel (**pre**, dotted line). Trajectories driven by ICON one-moment inputs are shown in orange, and those driven by ICON two-moment inputs are shown in blue.

the mixed-phase regime is influential at cirrus temperatures as preexisting ice, and more sophisticated schemes (in this case "2M") may differ more from one another than less sophisticated ones (in this case "1M"). The most important takeaway here is that ice microphysics causes large differences in ice mass mixing ratio and ice crystal number, even with microphysical-dynamic feedbacks controlled.

3.2. Cloud Ice Differences Over Time

With trajectory output, q_i and N_i differences can be quantified not only statistically but also temporally. We next look at how quickly q_i and N_i diverge to help identify which processes are responsible. Δq_i (meaning ICON minus CLaMS-Ice differences hereafter) is calculated along both the one- and two-moment trajectories to generate time-dependent probability distributions of these differences at cirrus temperatures (Figures 5a and 5b). These differences are calculated for $T < 237$ K, and not all trajectories exist at cirrus temperatures for the same duration, so that the sample size is not equal across these distributions. Starting from the full set of approximately 20,000 trajectories, only about half exist at cirrus temperatures for more than 10 hr and only about a quarter for more than 40 hr (Figures 5c and 5d).

The majority of Δq_i values fall between ±10 ppmv for both schemes (Figures 5a and 5b), but for about 5% of the trajectories, Δq_i can become as large as ±100 ppmv for the one-moment trajectories and ±200 ppmv for the two-moment ones. ΔN_i values also mostly fall between ±10 L^{-1} (Figure 6a; Note that we only have ΔN_i from the two-moment setup.) But excursions from this mean difference tend to be much larger than they are for Δq_i with a few hundred trajectories exhibiting ΔN_i of ±1,000 L^{-1}. The rare and large Δq_i and ΔN_i values occur primarily right after crossing the 237-K level, indicating the importance of the representation of homogeneous nucleation. A second peak of large Δq_i later in trajectory duration may indicate the influence of sedimentation. We investigate these process representations in Section 4.1.

The large-magnitude Δq_i and ΔN_i tend also to be correlated along the two-moment trajectories (Figure 6b). When a model predicts a higher ice crystal number, it generally predicts more cloud ice mass. However, equivalent increases in ice crystal number generate different increases in cloud ice mass for the two models. If CLaMS-Ice predicts 10 crystals L^{-1} more than ICON, it predicts roughly 10 ppmv more ice mass than ICON (i.e., $|\Delta q_i|/\log_{10}|\Delta N_i| = 9.2$ ppmv in quadrant III, $r^2 = 0.47$). If ICON predicts 10 crystals L^{-1} more than CLaMS-Ice, it predicts roughly 30 ppmv more ice mass than CLaMS-Ice. These sensitivities suggest that the representation of

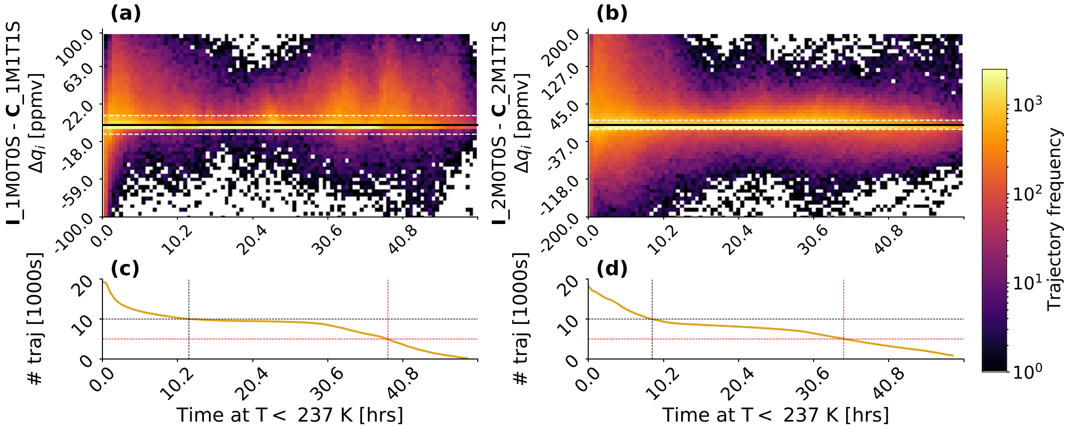

Figure 5. The largest cloud ice mass differences between the two microphysics models occur right after crossing the 237-K level. Probability distributions over time of Δq_i between Icosahedral Non-hydrostatic Model and CLaMS-Ice trajectories for the one- (panel a) and two-moment (panel b) inputs. The zero line is marked in black and ±10 ppmv is marked with white dashed lines. Note that the y-axis in panel (b) is two times larger than that in panel (a) Sample size over time is also shown with the 50th and 25th percentile in black and red to ease comparison (panels c and d).

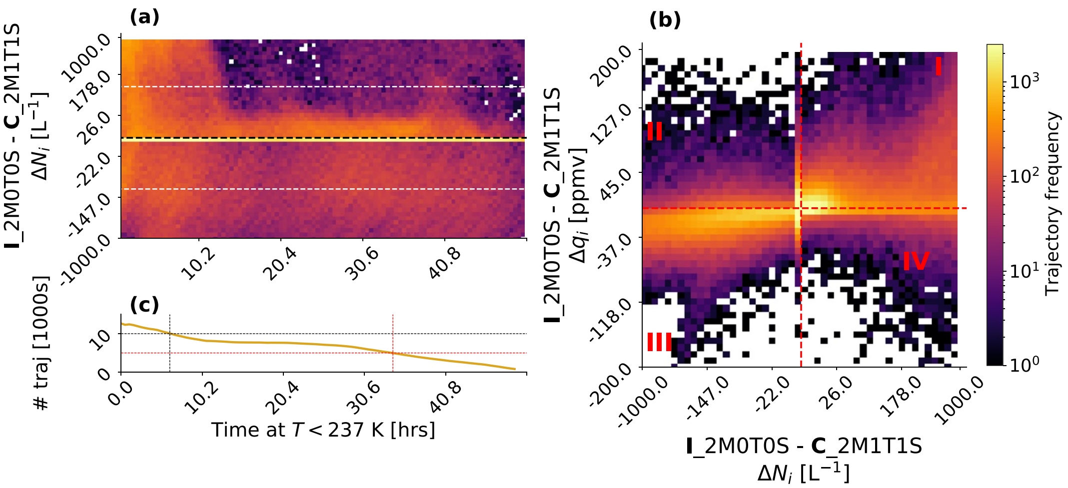

Figure 6. The largest magnitude ice crystal number differences also occur after traversing the 237-K level and are highly correlated with cloud ice mass differences. Probability distributions over time of ΔN_i between Icosahedral Non-hydrostatic Model and CLaMS-Ice trajectories for the two-moment inputs (panel a). The zero line is marked in black and ±100 L^{-1} is marked with white dashed lines. Sample size over time is also shown with the 50th and 25th percentiles in black and red to ease comparison (panel c). 2D histogram of ICON-CLaMS-Ice ΔN_i versus the corresponding Δq_i for the two-moment setup (panel b). Quadrant numbers and zero lines for both axes are marked in red. The colorbar is the same for panels (a and b).

depositional growth or the mass at which crystals are initialized may also be influential in producing the simulated spread in q_i and N_i values.

Finally, with the time dimension resolved, we evaluate the longest duration of non-negligible cloud ice mass at cirrus temperatures for the different trajectories, as a proxy for ***ice cloud lifetime***. We identify continuous sequences along the trajectories where $T < 237$ K and $q_i > 10^{-8}$ g kg^{-1} (as in Section 3.1). The cloud lifetime along a given trajectory is taken to be the longest of these continuous sequences. We use this longest sequence first because more than half of our trajectories have only one such sequence of non-negligible cloud ice mass values and second because these longest lived clouds will dominate lifetime accumulated radiative heating. In distributions of these lifetimes, we find that the ICON two-moment trajectories have by far the longest mean lifetime (8.29 hr, Figure 7). The CLaMS-Ice one- and two-moment trajectories have mean cloud lifetimes less than half as long (≈3 hr). We use these values for radiative heating scalings in Section 5.

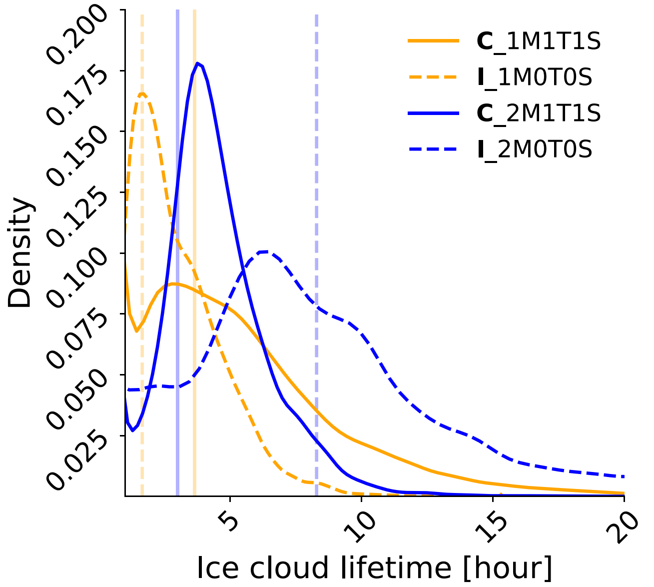

Figure 7. The longest ice cloud lifetimes occur in the Icosahedral Non-hydrostatic Model two-moment trajectories. Density distributions of ice cloud lifetime along the trajectories, evaluated as the longest duration of values with cirrus temperatures ($T < 237$ K) and non-negligible cloud ice mass ($q_i > 10^{-8}$ g kg^{-1}).

3.3. Cloud Ice Differences Versus Temperature and Humidity

We lastly look at where q_i variations occur as functions of temperature (T) and relative humidity with respect to ice (RH$_i$). The ice water content-temperature space has been established as a means of identifying cirrus origin, comparing cirrus from different geographical regions, and evaluating model output relative to in situ measurements (e.g., Heymsfield et al., 2017; Krämer et al., 2016, 2020; Luebke et al., 2013). In Figure 8, we compare the q_i-T parameter space from the CLaMS-Ice and ICON trajectories to an in situ tropical climatology, based upon work in Schiller et al. (2008) and ultimately incorporating data from five field campaigns. The trajectories exhibit good agreement with this in situ climatology: The majority of values in all setups fall within the spread of measured q_i as a function of T, and their means (denoted by **x**) fall close to the measured ones with only a slight underestimation.

While the model-measurement agreement is reasonable, the q_i-T spaces simulated along trajectories differ from one another greatly (Figure 8). These

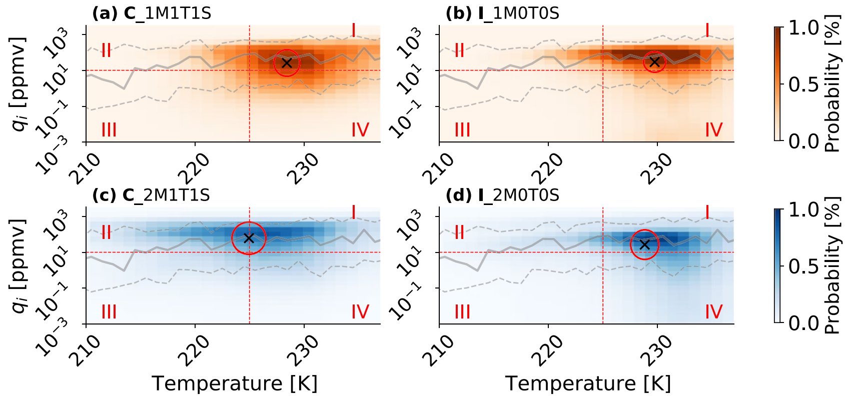

Figure 8. We can distinguish q_i-T dependencies along the trajectories with "quadrants," separating thicker and thinner ice cloud at colder and warmer cirrus temperatures. Two-dimensional probability distribution of ice mass mixing ratio q_i versus temperature T from the CLaMS-Ice (panels a and c) and Icosahedral Non-hydrostatic Model trajectories (panels b and d). Values from the one-moment setup are shown on top and from the two-moment setup on bottom. The in situ measurement climatology from Krämer et al. (2020) is overlaid in gray for all panels with the mean in a solid line and plus-minus a standard deviation in dashed lines. The distribution mean is marked with an **x**, standard deviations in T and q_i are encircled in solid red, and four quadrants are denoted with dashed red lines and Roman numerals.

differences occur despite the constrained flow field along the trajectories. The same is true of q_i-RH$_i$ spaces shown in Figure 9. To compare these thermodynamics spaces more concretely, we employ "quadrants," splitting the space into thicker and thinner ice cloud ($q_i >$ and <10 ppmv) at colder and warmer cirrus temperatures ($T >$ and <225 K) and at super- and subsaturation (RH $_i>$ and $<100\%$). Quadrant I represents, for example, thicker ice cloud at warmer cirrus temperatures or supersaturation, whereas quadrant III represents thinner ice cloud at colder cirrus temperatures or subsaturation. With this framework, the CLaMS-Ice two-moment setup generates more cirrus at colder temperatures than the other simulations. The q_i-RH$_i$ spaces show that the vast majority of cloud ice mass along the trajectories exists within ±2% of saturation; however, supersaturation is far more rare for the ICON values. Dependence of ice formation on supersaturation must also differ dramatically between CLaMS-Ice and ICON.

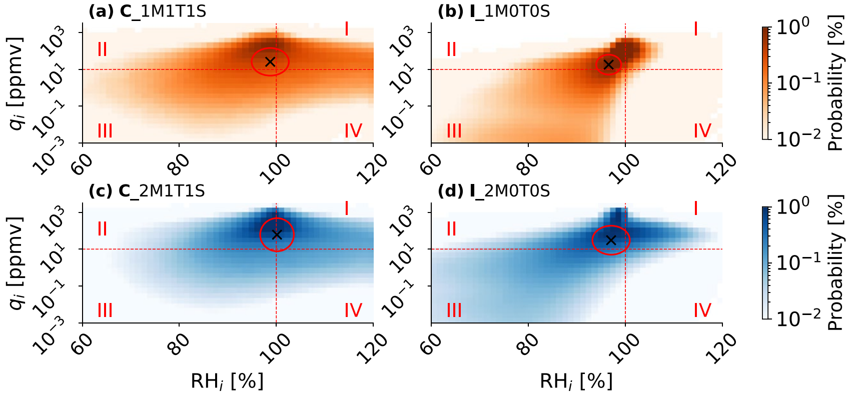

Figure 9. The Icosahedral Non-hydrostatic Model (ICON) trajectories are more subsaturated than the CLaMS-Ice ones, especially when cloud ice mass is small. Two-dimensional probability distribution of ice mass mixing ratio q_i versus relative humidity with respect to ice RH$_i$ from the CLaMS-Ice (panels a and c) and ICON trajectories (panels b and d). Values from the one-moment setup are shown on top and from the two-moment setup on bottom. The distribution median is marked with an **x**, standard deviations in RH$_i$ and q_i are encircled in solid red, and four quadrants are denoted with dashed red lines and Roman numerals.

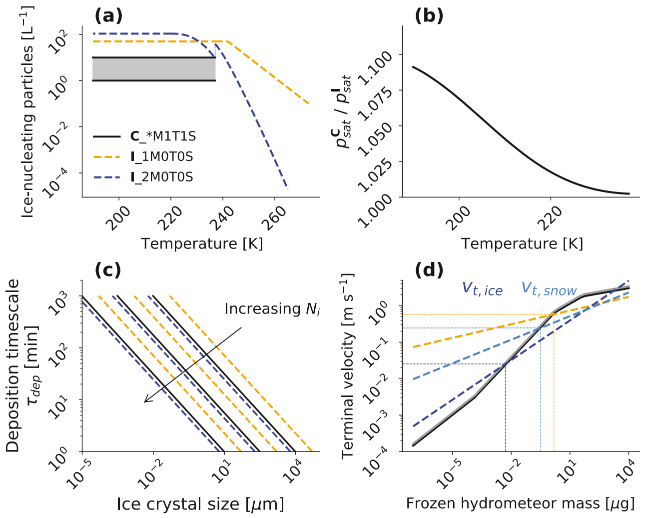

Figure 10. Microphysical variables differ between the two models for all phases of the ice cloud lifecycle. Ice-nucleating particle (INP) concentrations as a function of temperature (panel a). As CLaMS-Ice operates only for $T < 235$ K, its INP numbers are given by the corresponding Icosahedral Non-hydrostatic Model setup for $T > 235$ K Saturation vapor pressure over water (p_{sat}) as a function of temperature (panel b). p^{I}_{sat} are the p_{sat} values in ICON given by the widely used parameterization of Murphy and Koop (2005) and p^{C}_{sat} are the p_{sat} values in CLaMS-Ice given by recent measurements in Nachbar et al. (2019). Time scale for depositional growth (τ_{dep}) as a function of ice crystal size (panel c). The three sets of lines correspond to $N_i = 100$, 10, and 1 L^{-1} moving from bottom left to upper right, and a temperature of 225 K is assumed. Terminal velocity (v_t) as a function of ice crystal mass (panel d). For the ICON two-moment scheme, v_t of both ice and snow are shown in dark and lighter blue. Intersections are marked with dashed lines.

4. Process Decomposition of Cloud Ice Differences

4.1. Microphysical Formulations Throughout the Ice Cloud Lifecycle

In the analyses throughout Section 3, we have seen signatures of both heterogeneous (preexisting ice) and homogeneous nucleation, depositional growth, and sedimentation in generating spread in q_i and N_i, even with microphysical-dynamic feedbacks suppressed. Our previous work has illustrated the utility of process decomposition to understand variations in cloud ice mass, and hence cloud-radiative heating (Sullivan & Voigt, 2021). There, we employed an Eulerian perspective of limited-area ICON simulations and an altitudinal decomposition of processes. Here, we exploit the Lagrangian perspective of trajectories to temporally decompose microphysical processes with feedbacks constrained. The processes identified throughout Section 3 correspond to three lifecycle phases: formation (heterogeneous and homogeneous nucleation), development (depositional growth), and dissipation (sedimentation). We dissect their representation in CLaMS-Ice versus ICON below.

First, the ICON one- and two-moment schemes and CLaMS-Ice predict different numbers of ***ice-nucleating particles*** (INP) as a function of subzero temperature (Figure 10a, Table 2). In ICON, this INP number depends exponentially on temperature, whereas it is lognormally distributed between 1 and 10 L^{-1} in CLaMS-Ice, only when there is no preexisting ice (Table 2). The ICON one-moment scheme predicts several orders of magnitude more INP in the mixed-phase regime, supporting the idea from Section 3.3 that this setup is dominated by heterogeneous nucleation. ICON also permits heterogeneous nucleation as soon as supersaturation with respect to ice (s_i) develops, whereas CLaMS-Ice requires $s_i > 120\%$ (Table 2), explaining the differences in q_i-RH$_i$ space (Figure 9).

Then, the models differ in their representation of ***homogeneous nucleation***. The ICON one-moment scheme uses a very coarse representation of this process, simply freezing cloud droplets below a threshold temperature of 235 K. In the ICON two-moment scheme and CLaMS-Ice, supercooled sulfate solution particles freeze, following Koop et al. (2000):

$$\dot{q}_{i,\mathrm{hom}} = m_0 N_{SO4} \frac{\pi}{6} \overline{d}^{\,3}_{SO4} J(S_i, p_{i,sat}, p_{sat}) \tag{4}$$

where N_{SO4} is the number of sulfate solution particles, $\overline{d}_{SO4}$ is the mean diameter of these solution particles, and J is the homogeneous nucleation rate coefficient. If the solution particles are in equilibrium with their environment, J can be assumed to depend only on pressure and temperature through the saturation with respect to ice (S_i) and the saturation vapor pressures with respect to ice and liquid water ($p_{i,sat}$ and p_{sat} respectively) (e.g., Baumgartner et al., 2022; Koop, 2015).

N_{SO4} differs between the two models (Table 2), but previous work indicates that ice crystal number is only a weak function of solution particle number (e.g., Barahona & Nenes, 2008; Jensen & Toon, 1995; Liu & Shi, 2018). $\overline{d}_{SO4}$ is also the same in ICON and CLaMS-Ice, so we focus on the inputs to the nucleation rate coefficient. While $p_{i,sat}$ can be measured directly and with high accuracy down to 170 K, uncertainties remain in the ***saturation vapor pressure over liquid*** at temperatures colder than about 260 K (Murphy & Koop, 2005; Nachbar et al., 2019). Recent experimental work suggests that supercooled liquid water and amorphous solid water are distinct phases, a finding that implies higher p_{sat} values than those in widely used parameterizations for $T < 230$ K. These higher p_{sat} values are used in CLaMS-Ice but not in ICON (Figure 10b), explaining the larger q_i soon after the trajectories cross the 237-K level in Figure 5, as well as the q_i values at colder temperatures in the q_i-T space of Figure 8.

Table 2

Microphysical Parameters of CLaMS-Ice and Icosahedral Non-Hydrostatic Model Setups Grouped by Lifecycle Phase; Δt Is Time Step, MAX Refers to Thresholds Used, N_{INP} Is the Number of Ice-Nucleating Particles, m_0^{het} Is the Initial Mass of Heterogeneously Nucleated Crystals, $S_{i,c}^{het}$ Is the Critical Supersaturation With Respect to Ice for Heterogeneous Nucleation, N_{SO4} Is the Number of Sulfate Solution Particles, $\bar{d}_{SO4}$ Is the Mean Diameter and σ_{SO4} the Spread of the Sulfate Solution Particle Size Distribution, C Is Capacitance, α_d Is the Deposition Coefficient, $\mathcal{D}_v$ Is the Diffusivity of Water Vapor in Air, ρ_i Is the Bulk Ice Density, and v_t Is Hydrometeor Terminal Velocity

		CLaMS-Ice	ICON-2M	ICON-1M
Numerics	Δt	$\leq$24 s	24 s	24 s
	MAX	$N_{i,\mathrm{MAX}}^{\mathrm{hom}} \leq N_{\mathrm{SO4}}$	$N_{i,\mathrm{MAX}}^{\mathrm{hom}} \leq 5{,}000\ \mathrm{L}^{-1}$	$m_{i,\mathrm{MAX}} \leq 10\ \mu\mathrm{g}$ or
		No $d_{i,\mathrm{MAX}}$	$d_{i,\mathrm{MAX}} \leq 200\ \mu\mathrm{m}$	$d_{i,\mathrm{MAX}} \leq 200\ \mu\mathrm{m}$
Formation	N_{INP}	LN(1 L^{-1}, 0.9)	$\propto e^{-(T-T_{\min})}$	$\propto e^{-(T-T_{\min})}$
	m_0^{het}	10^{-15} kg	10^{-14} kg	10^{-12} kg
	$S_{i,c}^{\mathrm{het}}$	120%	100%	100%
	N_{SO4}	300 cm^{-3}	Tegen et al. (1997)	–
	$\bar{d}_{\mathrm{SO4}}$	25 μm	25 μm	–
	σ_{SO4}	1.4 μm	–	–
	p_{sat}	NDL19	MK05	MK05
Development	C	$C(a, b)$	$2r_i$	$2r_s/\pi$
	α_d	0.5	0.5	0.5
	$\mathcal{D}_v$	$2.11 \times 10^{-5}\ T^{1.94}/p$	$8.76 \times 10^{-5}\ T^{1.81}/p$	2.22×10^{-5}
	ρ_i	810 kg m^{-3}	916.7 kg m^{-3}	500 kg m^{-3}
Dissipation	v_t	$\alpha\,(m_i)\,m_i^{\beta(m_i)}$	αm_i^{β}	αm_s^{β} (snow only)

Note. MK05 stands for the Murphy and Koop (2005) parameterization and NDL19 for the Nachbar et al. (2019) one.

After crystal formation, the ice cloud develops through aggregation and growth from the vapor phase. We synthesize the effect of relevant parameters in diffusion-limited growth within a ***vapor deposition time scale*** (τ_{dep}) (e.g., Köhler & Seifert, 2015):

$$\tau_{dep} = \frac{1}{\dot{q}_{i,dep}} (q_v - q_{v,sat,i}) \tag{5}$$

$$\dot{q}_{i,dep} = \frac{8\pi C \mathcal{D}_v r_i N_i}{1 + H_i} (q_v - q_{v,sat,i}) \tag{6}$$

Where $\mathcal{D}_v$ is diffusivity of water vapor in air, C is capacitance, and H_i is the Howell factor to account for temperature differences between the environment and the ice crystal surface. For a given ice water content and crystal number, τ_{dep} is largest in the ICON one-moment scheme and smallest in the ICON two-moment scheme for a given ice crystal size, with CLaMS-Ice falling in between (Figure 10c). Faster growth in the ICON two-moment scheme is consistent with its higher $|\Delta q_i|/\log_{10}|\Delta N_i|$ in Figure 6b.

Finally, the cloud dissipates through sedimentation for which ***terminal velocity*** is the key parameter:

$$\dot{q}_{i,sed} = \frac{1}{\rho_a} \frac{\partial}{\partial z} (\rho_a q_i v_t) \tag{7}$$

All models calculate v_t as a power law of hydrometeor mass. While the power-law coefficients are themselves mass-dependent in CLaMS-Ice, they are constants in ICON (Table 2). In the one-moment scheme, only snow sediments but with the largest v_t of all three schemes for most hydrometeor masses (Figure 10d). v_t in the ICON two-moment scheme is larger than that in CLaMS-Ice for both the smallest and largest crystals ($m_i < 10^{-2}$ and $>10^2$ μg).

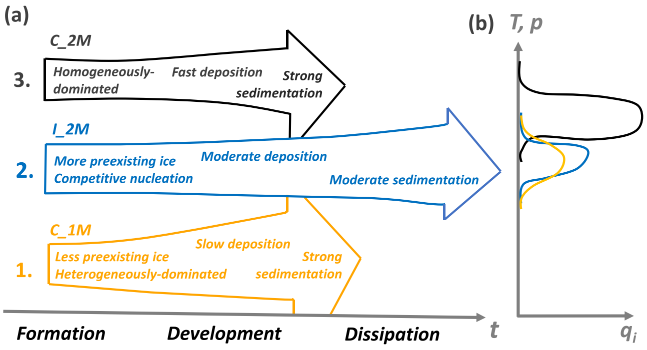

Figure 11. We propose three characteristic ice cloud lifecycles corresponding to trajectory output from the different microphysical schemes. Panel a shows the process strength for these three lifecycles during cloud formation (nucleation), development (depositional growth), and dissipation (sedimentation). **1**. is a *weak source-strong sink* lifecycle in orange corresponding to the CLaMS-Ice trajectories with one-moment inputs (**C**_1M); **2**. is a *strong source-weak sink* lifecycle in blue corresponding to the Icosahedral Non-hydrostatic Model trajectories with two-moment inputs (**I**_2M); and **3**. is a *strong source-strong sink* lifecycle in black corresponding to the CLaMS-Ice trajectories with two-moment inputs (**C**_2M). The length of the arrows is roughly proportional to cloud lifetime, but the shape of the areas does not reflect anything. Their vertical ordering corresponds roughly to the altitudes where the lifecycle is active. Panel b shows qualitative q_i profiles for each of these lifecycles.

The ease with which we can map differences in formulation onto the results in Section 3 indicates how influential various microphysical parameters are. Based upon the discussion above, we identify the number of ice-nucleating particles in the mixed-phase regime and the initial mass of these crystals (which determines both τ_{dep} and v_t) as parameters of primary importance and the saturation vapor pressure over liquid at very cold temperatures as a parameter of secondary importance. Our investigation of process formulations here has been detailed, but we next summarize the implications into three cloud lifecycles.

4.2. Three Characteristic Ice Cloud Lifecycles

The variations in ice cloud properties and microphysical formulations above lead us to propose three ice cloud lifecycles. No lifecycle is proposed corresponding to the ICON one-moment trajectories, as ice crystal number is not tracked along these, making them somewhat harder to characterize. First, the CLaMS-Ice trajectories using one-moment inputs are characterized by a ***weak source-strong sink*** lifecycle (**1.** in Figure 11a). Heterogeneous nucleation dominates initial ice formation, as ice-nucleating particles are abundant in the mixed-phase regime and supersaturation is not required. Despite slower depositional growth, the fewer, larger crystals sediment more easily, and less preexisting ice exists at cirrus temperatures. q_i and N_i values remain small and cirrus lifetime is shortest.

Then the ICON two-moment trajectories are characterized by a ***strong source-weak sink*** lifecycle (**2.** in Figure 11a). A combination of homogeneous and heterogeneous nucleation fuel initial ice formation. Ice-nucleating particles are less abundant at mixed-phase temperatures and still without a supersaturation requirement, but the threshold for homogeneous nucleation is now also reduced (via a lower p_{sat}). The crystals nucleate at a smaller initial mass and thus grow and sediment more slowly, prolonging cirrus lifetime.

Finally, the CLaMS-Ice trajectories using two-moment inputs are characterized by a ***strong source-strong sink*** lifecycle (**3.** in Figure 11a). Homogeneous nucleation dominates ice formation, as ice-nucleating particles are much less abundant over the full temperature range. A large number of crystals in combination with a fast depositional time scale facilitate growth. Fast growth means that sedimentation can dissipate the cloud quickly, shortening cirrus lifetime in this case.

5. Radiative Implications

We began with the motivation of using the constrained inputs and different microphysics schemes along the trajectories to provide bounds for cloud-radiative heating. q_i and N_i statistics (Section 3.1), cloud lifetime (Section 3.2), and cloud temperature depth (Section 3.3) provide all the necessary values to approximately scale $\mathcal{H}$ for the three proposed lifecycles. We finish our analysis by scaling longwave heating according to emissivity and shortwave heating according to albedo, for an assumed ice absorption cross section and lapse rate (Appendix A, Table 3).

The *strong source-weak sink* lifecycle generates the largest accumulated longwave heating ($\mathcal{H}_{\mathrm{LW}}t$), due both to its larger ice water path and longer lifetime. Its $\mathcal{H}_{\mathrm{LW}}t$ is 3.6 times that of the *strong source-strong sink* lifecycle and five times that of the *weak source-strong sink* lifecycle. If we omit cloud lifetime and calculate ratios of instantaneous longwave heating, we get a maximum 1.6 difference between the lifecycles. From such scalings in limited-area simulations, we obtained a 2-fold difference between one-versus two-moment schemes (Sullivan & Voigt, 2021). As for the distributions of q_i and N_i then, the trajectories indicate that structural differences in ice microphysics are sufficient to generate such a spread.

The relative spread in the shortwave heating scalings is larger than that in the longwave heating, given the direct rather than exponential proportionality to optical depth. While the relative spread in accumulated shortwave heating ($\mathcal{H}_{\mathrm{SW}}t$) is larger, the magnitude of $\mathcal{H}_{\mathrm{SW}}t$ is smaller, so that its absolute spread is likely smaller as well. As

Table 3

Input Parameters and Relative Scaling of Cloud-Radiative Heating in Longwave and Shortwave for the Three Proposed Lifecycles

	Accumulated longwave heating			
Lifecycle	$\overline{T}$	ΔT	IWP	t
1	228.4 K	2.4 K	5.55 g m^{-2}	3.01 hr
2	228.8 K	2.6 K	16.19 g m^{-2}	8.29 hr
3	224.9 K	3.1 K	7.04 g m^{-2}	3.65 hr

	Accumulated shortwave heating			
Lifecycle	D_e	ω	g	τ
1	14.63 μm	0.678	0.854	0.696
2	5.03 μm	0.711	0.821	1.62
3	9.18 μm	0.695	0.836	0.704
1/2	$(\mathcal{H}_{\mathrm{LW},1}t_1)/(\mathcal{H}_{\mathrm{LW},2}t_2) = 0.193$		$(\mathcal{H}_{\mathrm{SW},1}t_1)/(\mathcal{H}_{\mathrm{SW},2}t_2) = 0.0970$	
1/3	$(\mathcal{H}_{\mathrm{LW},1}t_1)/(\mathcal{H}_{\mathrm{LW},3}t_3) = 0.695$		$(\mathcal{H}_{\mathrm{SW},1}t_1)/(\mathcal{H}_{\mathrm{SW},3}t_3) = 0.565$	
2/3	$(\mathcal{H}_{\mathrm{LW},2}t_2/(\mathcal{H}_{\mathrm{LW},3}t_3) = 3.60$		$(\mathcal{H}_{\mathrm{SW},2}t_2)/(\mathcal{H}_{\mathrm{SW},3}t_3) = 5.82$	

Note. **1**: Weak-source, strong-sink; **2**: strong-source, weak-sink; **3**: strong-source, strong-sink. $\overline{T}$ is the mean cloud altitude, ΔT is the temperature depth of the cloud, IWP is the ice water path, t is mean cloud lifetime, D_e is the equivalent diameter of ice crystals, ω is the single-scattering albedo, g is the asymmetry parameter, and τ is the optical depth.

for the accumulated longwave heating, the largest accumulated shortwave heating value comes from the *strong source-weak sink* lifecycle, 10 times that from the *weak source-strong sink* lifecycle and six times that from the *strong source-strong sink* lifecycle. Omitting cloud lifetime again, the instantaneous shortwave heating varies by a maximum factor of 2.5 from one scheme to another. The hierarchy of $\mathcal{H}_{\mathrm{SW}}t$ is driven primarily by optical depth differences but also by larger single-scattering albedos and lower asymmetry parameter from the smaller mean crystal sizes in the *strong source-weak sink* lifecycle (Table 3). While the shortwave scaling values change with the spectral range chosen, their ranking and order of magnitude do not.

6. Conclusions

We have shown here that trajectories provide a kind of "Lagrangian piggybacking" to constrain microphysical-dynamic feedbacks and deconvolute the direct and indirect effects of changing microphysical schemes. We find here that structural differences in *ice-only* microphysics scheme are sufficient to generate about a 5-fold difference in q_i and N_i. In contrast, use of temperature fluctuations to mimic gravity waves and a pseudo-turbulent mixing tendency have relatively little impact on the output q_i and N_i. Interestingly, two detailed schemes (ICON two-moment and CLaMS-Ice) actually diverge more than one simple and one detailed scheme (ICON one-moment and CLaMS-Ice), perhaps because of the expanded parameter space.

This "Lagrangian piggbacking" technique provides a more fine-grain picture of the microphysics-only effect on cloud lifecycle than normal piggybacking because of the high temporal resolution of trajectories. We use this aspect in difference distributions over time that indicate the importance of the homogeneous nucleation threshold; the largest scheme-to-scheme deviations in q_i and N_i occur right after traversing the 237-K level. Because additional microphysics schemes can be run offline with the trajectory output, techniques that would otherwise require significant model development, like tracking process tendencies over cloud lifetime, are also available. Here, such process tendencies highlighted the importance of heterogeneous nucleation in the mixed-phase regime as preexisting ice for cirrus.

Another advantage of this trajectory methodology is its isolation of the phenomenon of interest, in this case ice clouds. Relative to simulating a full limited-area domain in traditional piggybacking, "Lagrangian piggybacking" reduces the output volume and computational cost. Conversely, different formulations of sedimentation can complicate the interpretation of the trajectory output, and the initial model development effort is high in implementing a trajectory module. Computational efficiency versus physical realism in sedimentation characterizes the tradeoff between using "Lagrangian piggybacking" and nudging to control dynamics.

Along with this new trajectory methodology, we advocate for process decomposition as a means of understanding differences between schemes. Based on the analyses here, we propose three ice cloud lifecycles with distinct radiative signatures: *weak-localized source*, *strong-dispersed source*, and *strong-localized source* cirrus. These lifecycles are associated with distinct vertical profiles of cloud ice mass and cloud-radiative heating (Figure 11), with the largest longwave heating and shortwave heating from the *strong-dispersed source* clouds, due to both long lifetime and large optical depth. The "Lagrangian piggybacking" and proposed lifecycles open up a number of directions for future work. We hope to couple the trajectory output to an offline radiative transfer scheme in order to better constrain the associated $\mathcal{H}_{\mathrm{LW}}$ and $\mathcal{H}_{\mathrm{SW}}$ values. In this work, we are also unable to say which of the model setups produce the most realistic results. A follow-up study will take advantage of in situ measurements in the simulation domain to evaluate simulated profiles of both thermodynamic and microphysical variables. Finally, the utility of the proposed lifecycles should be investigated as a means of decomposing upper-level cloud-radiative heating profiles inferred from satellite records.

Appendix A: Radiative Heating Scalings

Cloud-radiative heating is given by the flux divergence:

$$\mathcal{H}_* = \frac{g}{c_p} \partial_p F_* \tag{A1}$$

$$F_{LW}^{\uparrow} = (1-\varepsilon) F_{LW}^{\uparrow}\left(T_{\mathrm{bottom}}\right) + \varepsilon \sigma T_{\mathrm{top}}^4 \tag{A2}$$

$$F_{SW}^{\uparrow} = \alpha F_{\mathrm{solar}} = \omega (1-g) \tau F_{\mathrm{solar}} \tag{A3}$$

Where g is gravitational acceleration, c_p is the heat capacity at constant pressure, and F denotes a flux (W m^{-2}). The upwelling longwave flux is the reemitted portion of the longwave flux entering at cloud base (T_{bottom}) plus the emission at the cloud top temperature (T_{top}, Equation A2). The upwelling shortwave flux is the reflected portion of the solar flux impinging on the cloud. In this set of equations, cloud emissivity (ε) and albedo (α) are the key parameters determining the longwave and shortwave heating respectively. The plane albedo is approximately equal to the product of the single-scattering albedo (ω), one minus the asymmetry parameter (1-g), and the optical depth (τ).

We then scale longwave heating accumulated over the cloud lifetime using emissivity for two different microphysics scheme j and k:

$$\begin{aligned} \frac{\mathcal{H}_{\mathrm{LW},j} t_j}{\mathcal{H}_{\mathrm{LW},k} t_k} \sim \frac{\varepsilon_j t_j}{\varepsilon_k t_k} &= \frac{\left[1-\exp\left(-\tau_j\right)\right] t_j}{\left[1-\exp\left(-\tau_k\right)\right] t_k} \\ &= \frac{\left[1-\exp\left(-\kappa_i \int q_{i,j}\left(T_j\right) \Gamma^{-1} dT_j'\right)\right] t_j}{\left[1-\exp\left(-\kappa_i \int q_{i,k}\left(T_k\right) \Gamma^{-1} dT_k'\right)\right] t_k} \end{aligned} \tag{A4}$$

Here, dT_*' is the temperature depth of the ice cloud, t_* is cloud lifetime, κ_i is the absorption cross section of ice, and Γ is lapse rate. We assume that the absorption cross section of ice is independent of temperature and pressure and that a lapse rate of 6.5 K km^{-1} characterizes the cloud. We calculate the mean and standard deviation of temperature from the two-dimensional q_i-T distributions (Figure 8) and use $\bar{T} \pm 0.5\sigma_T$ as the integration bounds in temperature. Changing the integration bounds in temperature alters the IWP and τ values but does not qualitatively change our results. We fit $q_i(T)$ quadratically between the temperature bounds; higher-order fittings converge to an IWP within ±1% of the quadratic fit. As described at the end of Section 3.2, lifetime is calculated as the mean length of the longest sequences of non-negligible cloud ice values ($q_i > 10^{-8}$ g kg^{-1}) over all trajectories.

We scale shortwave heating accumulated over cloud lifetime using albedo for two different microphysics scheme j and k:

$$\frac{\mathcal{H}_{\mathrm{SW},j} t_j}{\mathcal{H}_{\mathrm{SW},k} t_k} \sim \frac{\alpha_j t_j}{\alpha_k t_k} = \frac{\omega_j (1-g_j) \tau_j t_j}{\omega_k (1-g_k) \tau_k t_k} \tag{A5}$$

The single-scattering albedo and asymmetry parameter are evaluated with the size-dependent formulations in the Baum-Yang optical scheme (Baum et al., 2011):

$$1 - \omega = b_0 + b_1 D_e + b_2 D_e^2 + b_3 D_3^2 \tag{A6}$$

$$g = c_0 + c_1 D_e + c_2 D_e^2 + c_3 D_e^3 \tag{A7}$$

Coefficients are taken from the 3.077–3.846 μm shortwave spectral range ($\mathbf{b} = (0.316 \times 10^{-4}, 0.629 \times 10^{-4}, 0.124 \times 10^{-6}, -0.739 \times 10^{-9})$; $\mathbf{c} = (0.772, 0.658 \times 10^{-3}, -0.652 \times 10^{-6}, -0.108 \times 10^{-7})$), and the effective diameter is calculated as follows:

$$D_e = 167.6 q_i^{0.216} \tag{A8}$$

$$D_e = a \left[\frac{q_{i,med}}{N_{i,med}} \frac{\Gamma\left(\frac{\nu+1}{\mu}\right)}{\Gamma\left(\frac{\nu+2}{\mu}\right)} \right]^b \frac{\Gamma\left(\frac{3b+\nu+1}{\mu}\right)}{\Gamma\left(\frac{2b+\nu+1}{\mu}\right)} \tag{A9}$$

Where Equation A8 is used for the one-moment scheme; Equation A9 for the two-moment scheme; and a, b, ν, and μ are parameters of the gamma hydrometeor size distribution and mass-dimension power law relations in Seifert & Beheng (2006).

Data Availability Statement

All codes to reproduce figures from model output are available at https://github.com/sylviasullivan/ice-microp-rad-vis and postprocessed data is available in an online repository at https://doi.org/10.5281/zenodo.6601215 (Sullivan, 2022). No proprietary software has been used in this work. The ICON model source code is available upon request to icon@dwd.de. Postprocessing was performed with Jupyter Notebooks.

Acknowledgments

SS was funded by DFG project VO 1765/6-1 (TropiC) and both SS and AV were supported by the German Ministry of Education and Research (BMBF) and FONA: Research for Sustainable Development (www.fona.de) under Grant 01LK1509A. SS acknowledges the CONSTRAIN working group at KIT and the larger group of researchers and students in the NSF-PIRE project 1743753 whose ideas and feedback have greatly contributed to this work, particularly Blaž Gasparini. We thank the German Climate Computing Center (DKRZ, Hamburg) for computing and storage resources as part of projects 1131 and 1018. We thank two anonymous reviewers for their feedback that has greatly helped to improve this manuscript.

References

Barahona, D., & Nenes, A. (2008). Parameterization of cirrus cloud formation in large-scale models: Homogeneous nucleation. *Journal of Geophysical Research*, *113*(D11). https://doi.org/10.1029/2007JD009355

Baum, B. A., Yang, P., Heymsfield, A. J., Schmitt, C., Xie, Y., Bansemer, A., et al. (2011). Improvements to shortwave bulk scattering and absorption models for the remote sensing of ice clouds. *Journal of Applied Meteorology and Climatology*, *50*(5), 1037–1056. https://doi.org/10.1175/2010jamc2608.1

Baumgartner, M., Rolf, C., Grooß, J.-U., Schneider, J., Schorr, T., Möhler, O., et al. (2022). New investigations on homogeneous ice nucleation: The effects of water activity and water saturation formulations. *Atmospheric Chemistry and Physics*, *22*, 65–91. https://doi.org/10.5194/acp-22-65-2022

Boudala, F. S., Isaac, G. A., Fu, Q., & Cober, S. G. (2002). Parameterization of effective ice particle size for high-latitude clouds. *International Journal of Climatology*, *22*(10), 1267–1284. https://doi.org/10.1002/joc.774

Brabec, M., Wienhold, F. G., Luo, B. P., Vömel, H., Immler, F., Steiner, P., et al. (2012). Particle backscatter and relative humidity measured across clouds and comparison with microphysical cirrus modelling. *Atmospheric Chemistry and Physics*, *12*(19), 9135–9148. https://doi.org/10.5194/acp-12-9135-2012

Doms, G., Förstner, J., Heise, E., Herzog, H.-J., Raschendorfer, M., Schrodin, R., et al. (2005). *A description of the nonhydrostatic regional model LM (Technical Report)*. Deutscher Wetterdienst.

Fan, J., Zhang, R., Li, G., & Tao, W.-K. (2007). Effects of aerosols and relative humidity on cumulus clouds. *Journal of Geophysical Research*, *112*(D14), D14204. https://doi.org/10.1029/2006jd008136

Gasparini, B., Rasch, P. J., Hartmann, D. L., Wall, C. J., & Dütsch, M. (2021). A Lagrangian perspective on tropical anvil cloud lifecycle in present and future climate. *Journal of Geophysical Research: Atmosphere*, *126*(4), e2020JD033487. https://doi.org/10.1029/2020jd033487

Grabowski, W. W. (2014). Extracting microphysical impacts in large-eddy simulations of shallow convection. *Journal of the Atmospheric Sciences*, *71*(12), 4493–4499. https://doi.org/10.1175/jas-d-14-0231.1

Grabowski, W. W. (2015). Untangling microphysical impacts on deep convection applying a novel modeling methodology. *Journal of the Atmospheric Sciences*, *72*(8), 2446–2464. https://doi.org/10.1175/jas-d-14-0307.1

Grabowski, W. W. (2019). Separating physical impacts from natural variability using piggybacking technique. *Advances in Geosciences*, *49*, 105–111. https://doi.org/10.5194/adgeo-49-105-2019

Grabowski, W. W., & Jarecka, D. (2015). Modeling condensation in shallow nonprecipitating convection. *Journal of the Atmospheric Sciences*, *72*(12), 4661–4679. https://doi.org/10.1175/jas-d-15-0091.1

Grabowski, W. W., & Morrison, H. (2016). Untangling microphysical impacts on deep convection applying a novel modeling methodology. Part II: Double-moment microphysics. *Journal of the Atmospheric Sciences*, *73*(9), 3749–3770. https://doi.org/10.1175/jas-d-15-0367.1

Grabowski, W. W., & Morrison, H. (2017). Modeling condensation in deep convection. *Journal of the Atmospheric Sciences*, *74*(7), 2247–2267. https://doi.org/10.1175/jas-d-16-0255.1

Haag, W., & Kärcher, B. (2004). The impact of aerosols and gravity waves on cirrus clouds at midlatitudes. *Journal of Geophysical Research*, *209*(D12), D12202. https://doi.org/10.1029/2004JD004579

Heymsfield, A., Krämer, M., Wood, N. B., Gettelman, A., Field, P. R., & Liu, G. (2017). Dependence of the ice water content and snowfall rate on temperature, globally: Comparison of in-situ observations, satellite active remote sensing retrievals, and global climate model simulations. *Journal of Applied Meteorology and Climatology*, *56*(1), 189–215. https://doi.org/10.1175/jamc-d-16-0230.1

Järvinen, E., Wernli, H., & Schnaiter, M. (2018). Investigation of mesoscopic complexity of small ice crystals in midlatitude cirrus. *Geophysical Research Letters*, *45*(20), 11465–11472. https://doi.org/10.1029/2018GL079079

Jensen, E. J., & Toon, O. B. (1995). Ice nucleation in the upper troposphere: Sensitivity to aerosol number density, temperature, and cooling rate. *Geophysical Research Letters*, *21*(18), 2019–2022. https://doi.org/10.1029/94gl01287

Kanji, Z. A., Ladino, L. A., Wex, H., Boose, Y., Burkert-Kohn, M., Cziczo, D. J., & Krämer, M. (2017). Overview of ice-nucleating particles. *Meteorological Monographs*, *58*, 1–33. https://doi.org/10.1175/AMSMONOGRAPHS-D-16-0006.1

Khaykin, S. M., Moyer, E., Krämer, M., Clouser, B., Bucci, S., Legras, B., et al. (2021). Persistence of moist plumes from overshooting convection in the Asian monsoon anticyclone. *Atmospheric Chemistry and Physics Discussions*. https://doi.org/10.5194/acp-2021-653

Kienast-Sjögren, E., Miltenberger, A. K., Luo, B. P., & Peter, T. (2015). Sensitivities of Lagrangian modelling of mid-latitude cirrus clouds to trajectory data quality. *Atmospheric Chemistry and Physics*, *15*(13), 7429–7447. https://doi.org/10.5194/acp-15-7429-2015

Köhler, C., & Seifert, A. (2015). Identifying sensitivities for cirrus modelling using a two-moment two-mode bulk microphysics scheme. *Tellus B: Chemical and Physical Meteorology*, *67*(24494), 24494. https://doi.org/10.3402/tellusb.v67.24494

Koop, T. (2015). Atmospheric water. *Proceedings of the International School of Physics, Enrico Fermi*.

Koop, T., Luo, B., Tsias, A., & Peter, T. (2000). Water activity as the determinant for homogeneous ice nucleation in aqueous solutions. *Nature*, *406*(6796), 611–614. https://doi.org/10.1038/35020537

Krämer, M., Rolf, C., Luebke, A., Afchine, A., Spelten, N., Costa, A., et al. (2016). A microphysics guide to cirrus—Part 1: Cirrus types. *Atmospheric Chemistry and Physics*, *16*(5), 3463–3483. https://doi.org/10.5194/acp-16-3463-2016

Krämer, M., Rolf, C., Spelten, N., Afchine, A., Fahey, D., Jensen, E., et al. (2020). A microphysics guide to cirrus—Part 2: Climatologies of clouds and humidity from observations. *Atmospheric Chemistry and Physics*, *20*(21), 12569–12608. https://doi.org/10.5194/acp-20-12569-2020

Lawson, R. P., Woods, S., Jensen, E., Erfani, E., Gurganus, C., Gallagher, M., et al. (2019). A review of ice particle shapes in cirrus formed in-situ and in anvils. *Journal of Geophysical Research*, *124*(17–18), 10049–10090. https://doi.org/10.1029/2018jd030122

Lee, K.-O., Dauhut, T., Chaboureau, J.-P., Khaykin, S., Krämer, M., & Rolf, C. (2019). Convective hydration in the tropical tropopause layer during the StratoClim aircraft campaign: Pathway of an observed hydration patch. *Atmospheric Chemistry and Physics*, *19*(18), 11803–11820. https://doi.org/10.5194/acp-19-11803-2019

Liu, X., & Shi, X. (2018). Sensitivity of homogeneous ice nucleation to aerosol perturbations and its implications for aerosol indirect effects through cirrus clouds. *Geophysical Research Letters*, *45*(3), 1684–1691. https://doi.org/10.1002/2017gl076721

Luebke, A. E., Avallone, L. M., Schiller, C., Meyer, J., Rolf, C., & Krämer, M. (2013). Ice water content of Arctic, midlatitude, and tropical cirrus—Part 2: Extension of the database and new statistical analysis. *Atmospheric Chemistry and Physics*, *13*, 6447–6459. https://doi.org/10.5194/acp-13-6447-2013

McKenna, D. S., Konopka, P., Grooß, J.-U., Günther, G., Müller, R., Spang, R., & Orsolini, Y. (2002). A new Chemical Lagrangian Model of the Stratosphere (CLaMS) 1. Formulation of advection and mixing. *Journal of Geophysical Research*, *107*(D16), 4309. https://doi.org/10.1029/2000jd000114

Miltenberger, A. K., Lüttmer, T., & Siewert, C. (2020). Secondary ice formation in idealised deep convection—Source of primary ice and impact on glaciation. *Atmosphere*, *11*(5), 542. https://doi.org/10.3390/atmos11050542

Miltenberger, A. K., Pfahl, S., & Wernli, H. (2013). An online trajectory module (version 1.0) for the nonhydrostatic numerical weather prediction model. COSMO. *Geoscientific Model Development*, *6*, 1989–2004. https://doi.org/10.5194/gmd-6-1989-2013

Morrison, H., van Lier-Walqui, M., Fridlind, A. M., Grabowski, W. W., Harrington, J. Y., Hoose, C., et al. (2020). Confronting the challenge of modeling cloud and precipitation microphysics. *Journal of Advances in Modeling Earth Systems*, *12*(8), e2019MS001689. https://doi.org/10.1029/2019ms001689

Murphy, D. M., & Koop, T. (2005). Review of the vapour pressures of ice and supercooled liquid water for atmospheric applications. *The Quarterly Journal of the Royal Meteorological Society*, *131*(608), 1539–1565. https://doi.org/10.1256/qj.04.94

Nachbar, M., Duft, D., & Leisner, T. (2019). The vapor pressure of liquid and solid water phases at conditions relevant to the atmosphere. *Journal of Chemical Physics*, *151*(064504), 064504. https://doi.org/10.1063/1.5100364

Nordeng, T. E. (1994). *Extended versions of the convective parametrization scheme at ECMWF and their impact on the mean and transient activity of the model in the tropics (Technical Report)*. ECMWF Tech. Memo.

Podglajen, A., Hertzog, A., Plougonven, R., & Legras, B. (2016). Lagrangian temperature and vertical velocity fluctuations due to gravity waves in the lower stratosphere. *Geophysical Research Letters*, *43*(7), 3543–3553. https://doi.org/10.1002/2016gl068148

Proske, U., Ferrachat, S., Neubauer, D., Staab, M., & Lohmann, U. (2021). Assessing the potential for simplification in global climate model cloud microphysics. *Atmospheric Chemistry and Physics Discussions*, *22*(7), 4737–4762. https://doi.org/10.5194/acp-22-4737-2022

Rosenfeld, D., Lohmann, U., Raga, G. B., O'Dowd, C. D., Kulmala, M., Fuzzi, S., et al. (2008). Flood or drought: How do aerosols affect precipitation? *Science*, *321*(5894), 1309–1313. https://doi.org/10.1126/science.1160606

Satoh, M., Stevens, B., Judt, F., Khairoutdinov, M., Lin, S.-J., Putman, W. M., & Düben, P. (2019). Global cloud-resolving models. *Current Climate Change Reports*, *5*(3), 172–184. https://doi.org/10.1007/s40641-019-00131-0

Schiller, C., Krämer, M., Afchine, A., Spelten, N., & Sitnikov, N. (2008). Ice water content of Arctic, midlatitude, and tropical cirrus. *Journal of Geophysical Research*, *113*(D24208), D24208. https://doi.org/10.1029/2008jd010342

Schumacher, C., Houze, R. A., & Kraucunas, I. (2004). The tropical dynamical response to latent heating estimates derived from the TRMM precipitation radar. *Journal of the Atmospheric Sciences*, *61*(12), 1341–1356. https://doi.org/10.1175/1520-0469(2004)061<1341:ttdrtl>2.0.co;2

Seifert, A., & Beheng, K. D. (2006). A two-moment cloud microphysics parameterization for mixed-phase clouds. Part I: Model description. *Meteorology and Atmospheric Physics*, *92*(1–2), 45–66. https://doi.org/10.1002/2014JD021917

Spichtinger, P., & Gierens, K. M. (2009). Modelling of cirrus clouds—Part 1a: Model description and validation. *Atmospheric Chemistry and Physics*, *9*(2), 685–706. https://doi.org/10.5194/acp-9-685-2009

Stevens, B., Acquistaoace, C., Hansen, A., Heinze, R., Klinger, C., Klocke, D., et al. (2020). The added value of large-eddy and storm-resolving models for simulating clouds and precipitation. *Journal of the Meteorological Society Japan*, *98*(2), 395–435. https://doi.org/10.2151/jmsj.2020-021

Sullivan, S. (2022). A Lagrangian perspective of microphysical impact on ice cloud evolution and radiative heating [postprocessed Dataset]. Retrieved from https://doi.org/10.1029/2022MS003226

Sullivan, S., & Voigt, A. (2021). Ice microphysical processes exert a strong control on the simulated radiative energy budget in the tropics. *Communications Earth and Environment*, *2*(1). https://doi.org/10.1038/s43247-021-00206-7

Tegen, I., Hollrig, P., Chin, M., Fung, I., Jacob, D., & Penner, J. (1997). Contribution of different aerosol species to the global aerosol extinction optical thickness: Estimates from model results. *Journal of Geophysical Research*, *102*(D20), 23895–23915. https://doi.org/10.1029/97jd01864

Voigt, A., Albern, N., & Papavasileiou, G. (2019). The atmospheric pathway of the cloud-radiative impact on the circulation response to global warming: Important and uncertain. *Journal of Climate*, *32*(10), 3051–3067. https://doi.org/10.1175/jcli-d-18-0810.1

Wedi, N. P., Polichtchouk, I., Dueben, P., Anantharaj, V. G., Bauer, P., Boussetta, S., et al. (2020). A baseline for global weather and climate simulations at 1-km resolution. *Journal of Advances in Modeling Earth Systems*, *12*(11), e2020MS002192. https://doi.org/10.1029/2020MS002192